RSC Applied Interfaces

ROYAL SOCIETY OF CHEMISTRY

PERSPECTIVE

View Article Online
View Journal | View Issue



Cite this: *RSC Appl. Interfaces*, 2025, **2**, 620

# Promoting combined AFM-electrochemistry techniques for analysis of charge transport at grain boundaries of ceramic components in electrochemical cells

K. Neuhaus, *[a] P. Mowe [a] and M. Winter [ab]

For decades, the differences between the transport properties of grains and grain boundaries in polycrystalline oxides have been widely discussed in the scientific community. The reason is that grain boundaries, although representing a much smaller fraction of a given material than the grain interior, can greatly influence the performance of ceramic materials, which is a major drawback for the industrial application of these materials. Detailed knowledge of the chemical and physical parameters at the interfaces between adjacent grains is required in order to develop targeted synthesis strategies that specifically influence the transport properties of grain boundaries. Atomic force microscopy (AFM)-based electrochemical methods use an nm-sized tip as a probe and are able to image, for example, band bending at grain boundaries or variations in electrical conductivity with extremely high local resolution, thus providing small-scale insights into the physical and electrochemical conditions at grain boundaries. The results obtained by AFM-based electrochemical experiments are complementary to conventional electrochemical measurements and facilitate detailed modeling of grain boundary parameters in different materials. In this work, the differences between grain boundaries and grain interiors with respect to charge transport properties are first discussed with a special focus on oxide ion conducting and proton conducting materials. In a second step, a broader perspective on current research and potential applications of AFM-based grain boundary analysis in the field of lithium-ion battery materials is given.

Received 20th September 2024,
Accepted 6th March 2025

DOI: 10.1039/d4lf00325j

rsc.li/RSCApplInter



## 1 Introduction

Atomic force microscopy (AFM) is a measurement technique which was invented by Binnig, Quate and Gerber in 1986.[1] It evolved from scanning tunneling microscopy and can primarily be used to measure the topography of a given sample. Basically, a very fine tip with a diameter in the range of a few nm, which is attached to a cantilever, is scanned along a sample surface. The position of the cantilever is controlled by a laser positioning system where a laser beam is reflected off the back of the cantilever, and the reflection is then captured by a photodetector. The possible resolution for AFM topography measurements depends on the tip diameter, but is typically in the nm range in the $x$ and $y$ directions and in the pm range in the $z$ direction. By monitoring the tilt and torsional motion of the cantilever and tip, additional information about the surface roughness and elasticity can be obtained.

AFM measurements are possible in three basic modes: i) contact mode, where the tip remains in contact with the sample surface throughout the whole experiment, ii) intermittent contact mode, where the cantilever vibrates at its resonance frequency (typically in the kHz-range) and taps the sample surface at regular intervals during scanning, and iii) non-contact mode, where the tip is moved at a constant distance above the surface, allowing interaction between the tip and short-range physical attractive and repulsive forces of the sample surface.[2]

The AFM technique has been rapidly diversified, for instance by the use of conductive AFM tips, which allow to image different physical properties like electrical conductivity or local surface potential distribution and to correlated them with the sample topography. Due to the very high resolution, AFM-based methods are well-suited to measure a range of different parameters at very tiny interfaces and have been used more and more frequently in the last decade to shed light on the complex topic of charge carrier transport and defect concentrations at grain boundaries and similar interfaces.[3–5]

The present work focuses on AFM-based electrochemical methods and their application for measurements of grain

[a] *Forschungszentrum Jülich GmbH, Institute of Energy Materials and Devices IMD-4: Helmholtz-Institute Münster (HI MS), Münster, Germany. E-mail: k.neuhaus@fz-juelich.de*
[b] *University of Münster, MEET Battery Research Center, Institute of Physical Chemistry, Münster, Germany*

boundary related variations in transport behavior and defect concentrations in oxidic oxide-ion, proton, and lithium-ion conductors. Corresponding measurement techniques have already been successfully applied for example in the field of solar cell materials,[6,7] where grain boundaries play an important role in charge transport, although the focus here is on electron/hole transport rather than ion transport.

The overall goal of this perspective is, on the one hand, to show how valuable AFM-based electrochemical measurements can be for determining small-scale electrochemical interactions at very small interfaces. On the other hand, challenges and opportunities for AFM-based studies of charge transport at grain boundaries are identified.

## 2 Theoretical background and methods

### 2.1 Differences in transport characteristics between grain interior and grain boundaries

In a first instance, grain boundaries represent confined zones with a structural mismatch due to differing crystallographic orientations between adjacent grains. However, grain boundaries can have strongly different transport characteristics for ions and/or electrons compared to the bulk of a given material. This can have different reasons, which are discussed in the following sections.

**2.1.1 Space-charge layers.** The concept of space-charge layers (SCL) was first introduced by J. Frenkel in 1946.[8] SCL correspond to the charge carrier redistribution at space-charge regions which exist in the immediate vicinity of a two-phase contact. C. Wagner then extended the theory to explain how the contact of two semi-conductors affects the conductivity in the contact area.[9] T. Jow and J. B. Wagner further developed the concept to explain electrochemical peculiarities which occur at interfaces in ionic conductors.[10] Based on these initial findings, J. Maier and co-workers established comprehensive concepts for qualitative and quantitative determination of boundary effects and associated changes in defect concentration in ionic conductors.[11–18] These concepts are valid for dilute materials, *i.e.* ceramics with a very low dopant concentration and thus a very low charge carrier concentration. Here, SCL at grain boundaries arise due to the segregation of charged defects, such as oxygen vacancies or dopant ions, at the grain boundary regions. This segregation creates an electrostatic potential, leading to the formation of depletion or accumulation layers that influence ionic transport. In contrast to the relatively narrow crystallographic grain boundaries, which typically show a thickness of less than 10 nm, the space-charge layer can be considerably extended (>100 nm) depending on the material and charge carrier concentration.[19] The inhomogeneity in charge distribution has a strong effect on the charge transport characteristics along and across grain boundaries, which again is of crucial interest for the industrial application of ionic conductor materials in energy generation and storage devices.

The width of these space-charge layers is typically larger in low-dopant systems due to reduced screening effects, as fewer mobile charge carriers are available.[20,21] The description of dilute systems assumes constant defect mobilities in grain boundaries and grain interiors, whereby the defect concentrations differ. However, defect–defect or defect–dopant interactions are neglected here, which increasingly influence the transport properties at higher doping concentrations.[22] Various studies have already shown that the agreement between theory and experiment, which works quite well with dilute materials, is insufficient for higher dopant concentrations.[23,24] However, materials with low doping concentrations are not suitable for a range of applications such as fuel cells, battery storage or sensors due to their low ionic conductivity. D. S. Mebane and R. A. De Souza[25] were able to solve this problem and extended the theoretical framework to predict experimental point-defect behavior at grain boundaries in concentrated solid solutions. By combining the Poisson–Boltzmann approach to describe defect behavior near interfaces with the Cahn–Hilliard model for concentrated solid solutions they achieved good accordance between their model and experimental values from impedance spectroscopy measurements.

Impedance spectroscopy is the most common method for measuring the lateral extent of space-charge regions. Other possibilities to investigate dopant segregation[26] and also to directly observe local grain boundary potential barriers are transmission electron microscopy based methods (*e.g.* atom tomography).[27] Here, the advantage is the possible combination with measurements of the local chemical composition, but the disadvantages are the difficult sample preparation (ion beam milling, FIB lamellae preparation *etc.*) and high costs of the TEM instrumentation.

**2.1.2 Secondary phases at grain boundaries.** In addition to space-charge zones, the segregation of dopant ions leading to secondary phase formation at the grain boundaries as well as the accumulation of impurities such as $SiO_2$ (ref. 28) can also have a strong influence on electron and ion transport at grain boundaries (and also affect SCL formation). Secondary phases can increase or decrease the grain boundary potential barrier depending on their chemical nature. For example, insulating impurity phases often increase the barrier by trapping charge carriers, while conductive phases can reduce it by providing additional pathways for ionic or electronic transport. This has for example been exploited by adding transition metal oxides as sintering aids in doped ceria materials, which led to a drastic increase of electron partial conductivity at the grain boundaries,[29,30] promoting possible application in fuel cell electrodes.

Recently, S. Kim and co-workers[31] established an impedance spectroscopy-based method to determine the contribution of space-charge *vs.* insulating layers on the grain boundary resistivity in proton and oxide-ion conducting ceramic with low dopant concentrations. Apart from that, it is difficult to study the transport properties of individual grain boundary phases with conventional electrochemical

methods due to their very low thickness. For both dilute and high doping concentrations, but also for materials with secondary phases at the grain boundaries, AFM-based measuring methods are suitable as complementary techniques for analyzing the grain boundaries. On the one hand, they can act as a nanocontact for conventional electrochemical measurements due to their small contact diameter. On the other hand, special measuring methods such as Kelvin probe force microscopy (KPFM) or Electrochemical Strain Microscopy (ESM) can provide direct information about the height and width of the potential barrier at grain boundaries or enable high-resolution measurements of ionic conductivity. Details will be discussed in chapter 2.2 and 3.

**2.1.3 Effect of temperature.** Temperature is one factor that significantly affects ionic transport in general, and also space-charge layers in both dilute and non-dilute systems. As temperature increases, the mobility of ions and defects rises, reducing the potential barrier at grain boundaries and enhancing ionic conductivity. Additionally, the thickness of the space-charge layer decreases with temperature, following a Debye-like screening effect, where the layer thickness scales with the square root of temperature.[32] Elevated temperatures also promote defect diffusion, which can further modify the space-charge layer properties and improve ionic transport.[21]

Ceramic proton and oxide-ion conductors work at ideal operation temperatures between 400–900 °C. Since most AFM-based observations are conducted in a low-temperature regime, typically below 200 °C, or even at sub-room temperature, impedance spectroscopy measurements of ceramics can be performed at optimal operating temperatures. For materials with high application temperatures, AFM-based measurements at room temperature therefore only provide limited information, but can be used to complement measurements at the corresponding application temperatures. There are some AFM measurement setups that can also work at temperatures well above 200 °C,[33,34] but then there are problems with, for example, the conductive coating or the very fine AFM tips that cannot easily withstand these temperatures. Meanwhile, AFM-based measurement methods are ideally suited for battery materials that already exhibit very good conductivity within the range of ambient temperature.[35,36]

### 2.2 AFM-based electrochemical measurement techniques

AFM-based electrochemical measurements allow for measurement as well as visualization of different grain boundary characteristics (see also Fig. 1). For this kind of measurements, typically an AFM tip coated with Pt or Au is used to make it conductive. Other than in most conventional electrochemical measurement techniques which apply macroscopic electrodes, a conductive AFM tip offers the possibility to gather information on different parameters with a high lateral resolution and simultaneously correlate the results to topographical attributes of the sample. This means that grain boundaries can be easily identified on crystalline samples which have not undergone a surface treatment, as grain boundaries appear as small trenches in the topography (similarly as in light or electron microscopy images). In the following, the four most important AFM-based measurement techniques in this context will be broadly introduced. An overview can also be found in Table 1.

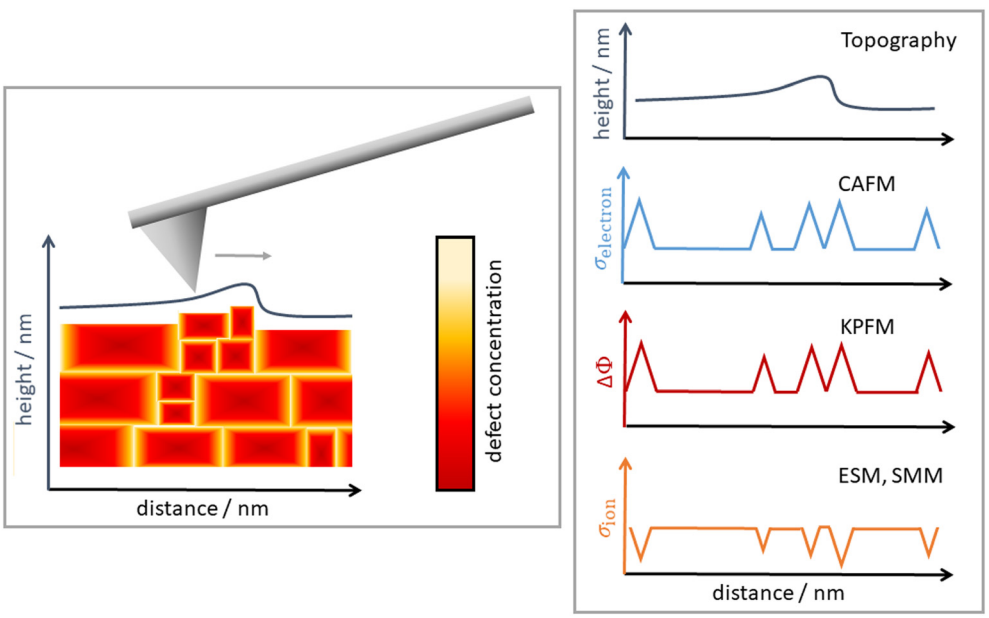


Fig. 1 Schematic overview of possibilities of grain boundary characterization using AFM-based measurement techniques. Right: The AFM tip is scanned over an idealized ceramic material with differently sized grains. The defect concentration varies from bulk to grain boundaries. Right: Apart from the sample topography, AFM-based analysis methods allow directly obtaining or calculating important physical characteristics associated with the defect concentration variations.

**2.2.1 Conductive AFM (CAFM).** The straightest way to gather information about local electrical conductivity of the sample is called current sensing AFM or conductive AFM (CAFM). For this technique, the sample is contacted with a large contact either on the top edge of the sample or on the backside of the sample. The AFM tip is used as second contact, which allows for mapping the electric current between both contacts, if a fixed potential is applied. Since mainly Pt or Au are used as conductive layer on the AFM tips, materials with low ionic and electronic conductivity (like the typical oxide-ion or proton conducting ceramic as Gd-doped ceria or $BaCeO_3$ at room temperature) can typically not be analyzed with this technique since the measured currents are too low.

**2.2.2 Electrochemical Strain Microscopy (ESM).** Electrochemical Strain Microscopy (ESM) is a relatively new atomic force microscopy technique which is especially well suited for investigating electrochemical reactivity and ionic flows in solids down to the nanometer scale.[36–38] It enables to investigate the change of surface morphology due to applying either a constant voltage or an increasing and decreasing voltage sweep and simultaneously measuring the strain of the material and possible particle growth. In the past, this technique has mainly been applied to $Li^+$ conductors,[39–43] but also transport phenomena in oxide ion conductors (among others) at room temperature were analyzed.[44–46]

ESM can be divided into two main spectroscopy methods, the time spectroscopy and the voltage spectroscopy. While in time spectroscopy the signal is measured after a short voltage pulse and normally is detected over a longer time, in voltage spectroscopy the signal is measured during each pulse of increasing and decreasing voltage.

It is possible to detect several different signals. Information about the surface are similar to other standard AFM techniques and are mainly described by the height and phase signal. The topography shows an image of the sample by scanning the surface with the AFM tip and depicts the differences in both lateral and height difference, the height information is directly connected to the change of the AFM z-piezo. The phase signal is sensitive to the stiffness of the surface as well as to the adhesion between tip and sample. Both signals (height and phase) are detected in intermitting contact mode (AC mode). The ESM amplitude signal gives information about the change of the strain while applying different bias pulses,[47] either with comparably low frequency or in the high frequency regime. This signal is detected while the AFM tip is directly in contact with the surface and is based on the deflection of the cantilever, which means that variations in the pm-range can be detected. An increasing ESM amplitude signal means that the surface height is increasing locally and *vice versa*.

Based on the assumption that ion transport processes in the sample material are diffusion-limited and that the contribution of migration is minimal, the amplitude of the oscillating surface displacement $A_{dis}$, in units of distance, is (in the high-frequency regime):

$$A_{dis} = 2(1+\nu)\beta\frac{V_{ac}}{\sqrt{\omega}}\cdot\frac{\sqrt{D}}{\eta} \quad (1)$$

Here, $V_{ac}$ is the a.c. voltage amplitude, $D$ the chemical diffusion coefficient, $\omega$ is the frequency of the applied field, and $\eta$ describes the linear relation between applied field and chemical potential. Coefficient $\beta$ is an effective Vegard coefficient, which expresses an (approximate) empirical linear relationship between lattice size and concentration of the ion, which is mobile in the material,[48] and can be determined by X-ray diffraction measurements.

**2.2.3 Kelvin probe force microscopy (KPFM).** Kelvin probe force microscopy (KPFM) is a scanning probe microscopy technique, which was invented by Nonnenmacher *et al.* in the early 1990s.[49,50] It enables observation of the topography of a sample in combination with the Volta potential with a resolution in the nm-range.[51–54] The KPFM technique offers a possibility to map potential differences associated with local changes in defect concentrations[51,55] and is therefore ideally suited to investigate space-charge layers at grain boundaries. KPFM is performed in intermittent contact mode with the cantilever vibrating at its resonance frequency. During the measurement, an AC potential with a certain frequency and amplitude is applied to the AFM tip. This AC potential is fixed by an additional external voltage $U_{DC}$ which compensates the contact potential difference between sample and probe tip[51] by setting the tip to the same potential according to

$$U_{KPFM} = -\frac{1}{e}\Delta\varphi_{CPD} = U_{DC} \approx \varphi \quad (2)$$

A plot of the potential $U_{DC}$ during the surface scan of the probe tip yields the KPFM image. The contact potential difference ($\Delta\varphi_{CPD}$) is proportional to the difference of the work functions of the metal coated AFM tip and the sample ($\Delta\varphi_{CPD} = \Delta\varphi_e$).

**Table 1** Overview over AFM-based measurement methods relevant for grain boundary characterization. A detailed description can be found in sections 2.2.1 to 2.2.4

| Technique | Common abbreviations | Measurand |
|---|---|---|
| Conductive AFM | CAFM, CS-AFM | Local electrical conductivity |
| Electrochemical strain microscopy | ESM | Change in surface morphology due to ion movement induced by applied voltage |
| Kelvin probe force microscopy | KPFM, KFM, SKPM | Local contact potential difference between metal coated tip and sample surface |
| Scanning microwave impedance microscopy | sMIM, SMM | Complex impedance → resistance |

$$\Delta\varphi_{CPD} = \varphi_{tip} - \varphi_{smp} \quad (3)$$

The work function is proportional to the difference in the Fermi energy levels of the tip and the sample. Therefore, changes in the defect concentration of the sample can be detected, assuming the work function of the tip is unchanged during the experiments.

The KPFM signal can be calibrated using a reference sample with a well-established work function like for example HOPG, thus yielding absolute values for the contact potential difference. Then, a correlation of the Volta potential at the probe location and surface Fermi energy $E_{FS}$ can be established by:

$$E_{FS} = E_{Vac} - V_{tip} - \varphi_{tip} \quad (4)$$

with $E_{Vac}$ = vacuum level. Still, even when no calibration is performed, the relative differences of Volta potential between different areas on the sample, which are proportional to changes in the surface-near defect chemistry, can be mapped with high resolution.

In many cases, KPFM studies are not executed in vacuum but in air, so an influence of adsorbed water and other adsorbed species on the measurement signal cannot be ruled out. Water acts as a dipole which can be aligned for example in an electric field and which can have an additional effect on the KPFM signal.[56]

**2.2.4 Impedance spectroscopy and related AFM-based methods.** There have been various attempts to combine impedance spectroscopy measurements with AFM measurements by using the AFM tip as one contact in a two- or three-electrode setup for "conventional" impedance spectroscopy measurements[57–59] This experimental setup has several drawbacks: i) as the measurement cell is asymmetrical and the AFM tip is very small compared to the back contact, the analysis of the resulting spectra is much more challenging. ii) Large tip-sample contact forces are necessary to ensure excellent tip-sample contact, but this leads to a fast wearing of the metallic coating of the tip.[58,59] However, the coating has to be completely intact, otherwise the contact resistance between tip and sample is determinant for the measurement results and the tip-surface coupling becomes capacitive. iii) Other than in many of the AFM-related measurement techniques, the method does not only probe the uppermost surface layers but has a certain penetration depth (complete length from AFM tip to back contact).

Apart from conventional impedance spectroscopy methods, there are two other impedance spectroscopy-related AFM-based methods: Keysight, USA and Oxford Instruments, UK offer Scanning Microwave Microscopy (SMM) and Scanning Microwave Impedance Microscopy (sMIM), respectively, which are measurement techniques utilizing an external microwave signal in the GHz range to measure the complex impedance of a sample. To achieve this, in contact mode, the signal is conducted through the AFM tip onto the surface of the sample and the diffracted signal is monitored. During scanning, local sample variations in permittivity ($\varepsilon$) and conductivity ($\sigma$) affect the reflected microwaves and can be analyzed. Typical penetration depths are in the range of 80 nm to 120 nm, depending on the materials. Respective techniques have already been used to measure charge carrier mobility in different semi-conductive materials or electrolytes[60,61] and even for observation of grain boundary characteristics in electron conductors such as solar cell materials[62] or ferrites,[63] but comprehensive studies on grain boundaries of ion conductive, oxidic materials are very scare so far. However, the measurement approach would be extremely interesting for a variety of different questions with relation to defect concentration distribution at grain boundaries.

# 3 AFM analysis of grain boundaries in oxide-ion and proton conductive oxides

Oxide ion conductive ceramics normally work at elevated application temperatures compared to those typically used for solid oxide electrolyzers, lithium ion batteries or semi-conductors. Typical temperatures range from 600–1000 °C with ceria-based materials at the low temperature end, perovskites like (La,Sr)(Co,Fe)$O_3$ (LSCF) and (Ba,Sr)(Co,Fe)$O_3$ (BSCF, see also Fig. 2) in the low to middle temperatures and yttria-stabilized zirconia (YSZ) at the high temperature end. Apart from very few exceptions,[33,34,64] these temperatures cannot be accessed by AFMs, hence AFM-based research has to focus on temperatures where the oxygen vacancies only show very low mobility or are completely frozen.[65,66] Nevertheless, near-surface defects can still be mobile and, for example, participate in catalytic reactions and proton conductivity in oxide-ion conductors also occurs at lower temperatures than oxide-ion conductivity.

There has not been much scientific work published with regards to AFM-based measurements specifically on proton conductive oxides. However, predominantly oxide-ion conductive materials like ceria and zirconia have shown to transport protons *via* the surface in the low to intermediate temperature regions.[67–70]

## 3.1 Perovskite proton and oxide ion conductors

Y-doped $BaZrO_3$ (especially the composition $BaZr_{0.9}Y_{0.1}O_{3-\delta}$) has one of the highest reported bulk proton conductivities compared with other perovskite materials (6.5 mS $cm^{-1}$ at 650 °C in wet air)[71] and it also shows a higher chemical and mechanical stability than corresponding cerate-based materials, especially when exposed to $CO_2$. Similar to the oxygen ion conductive materials described in section 5, $BaZrO_3$ and its acceptor-doped derivatives have been shown to develop a net positive charge at the grain boundaries with an adjacent negatively charged SCL. The positive charge at the grain boundary core is counteracted by segregation of the

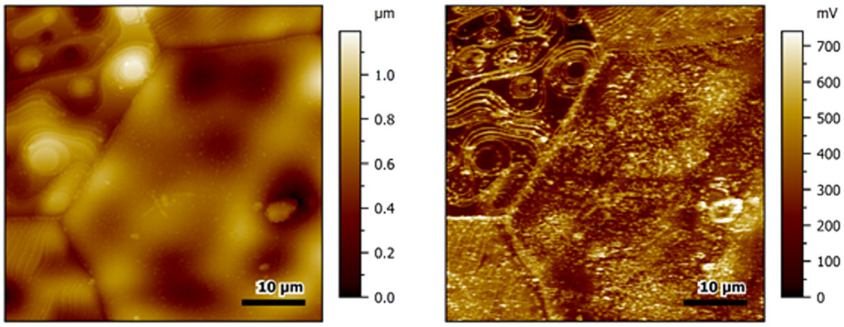


**Fig. 2** Topography (left) and corresponding KPFM image (right) of a $Ba_{0.5}Sr_{0.5}Co_{0.8}Fe_{0.2}O_3$ ceramic pellet with very large grains. The grain boundaries appear as lines with markedly increased potential and also step faults show light potential differences. Measurements were performed with PPP-NCSTPt tips in a single-pass amplitude modulation mode in lab air.

acceptor dopant, therefore a higher acceptor dopant concentration leads to a decreased potential barrier height at the grain boundaries, hence space-charge layers are mainly relevant for dilute defect concentrations. The situation is easily comparable to the one for oxide-ion conductive materials, as $BaZrO_3$ and related perovskite proton conductors also show oxide-ion conductivity at elevated temperatures.

Differences between the grain boundary potential barrier height calculated from eqn (1) under humid or dry conditions have been attributed to a grain boundary core hydration process (preferred absorption of protons at the grain boundary core defects when changing from dry to humid conditions).[71] Also, a strong influence of the synthesis conditions is reflected in differing potential height barriers found for materials with the same compositions but different synthesis routes.[71–74]

Specific measurements of the potential barrier at the grain boundaries under different conditions using AFM-based methods have so far (to the knowledge of the authors) not been performed for $BaZrO_3$-based materials, although the potential difference is high enough to make grains and grain boundaries easily distinguishable with AFM-based electrochemical measurement methods,[71–74] but there are two AFM-based studies on proton transport which also are of interest for fully understanding the grain boundary characteristics in $BaZrO_3$.

Yang *et al.*[75] performed ESM measurements to detect the electrochemical activity of fully hydrated $BaZr_{0.8}Y_{0.2}O_{3-\delta}$ thin films on $NdGaO_3$ substrates, which show a 10% lattice mismatch. Local electrochemical results were complemented with scanning transmission electron microscopy (STEM) investigations to obtain information about local structural defects. The investigations showed a clear dependence between the local conductivity and local structural defects (introduced by lattice mismatch of thin film and substrate) at temperatures between RT and 110 °C, which is in good accordance to the idea that grain boundaries are main obstacles for proton transport in Y-doped $BaZrO_3$. For the measurements, short polarization pulses with up to 42 V were used and the polarization–relaxation of the lattice strain was monitored using the local dilatation in *z*-direction. The obtained activation energies for samples with 300 nm film thickness were roughly comparable to literature results for the bulk transport (0.3 eV with ESM compared to roughly 0.4 eV obtained from literature by conventional electrochemical methods). Samples with a film thickness of 20 nm showed considerably decreased activation energies. This was attributed to a network of dislocations at the interface between thin film and substrate, which could increase the proton transport locally and have a major impact due to the low thickness of the film.

These findings are backed up by investigations by Ding *et al.*[76] using time-resolved KPFM on epitaxial $BaZr_{0.8}Y_{0.2}O_{3-\delta}$ thin films grown on MgO substrates. For their measurements, Ding *et al.* polarized their samples using sputtered micro contacts and performed a series of measurements before, during and after the polarization in order to measure polarization–relaxation effects on the surface potential. They were able to show that slightly Ba-deficient/Y-enriched thin films show a smaller local distortion accompanied by a decrease of proton-trapping effect and a higher proton mobility (Ba vacancies act as acceptor dopants on the A-side). Local enrichment of $Y^{3+}$ cations has also been observed at the grain boundaries in Y-doped $BaZrO_3$.

Apart from proton conducting perovskites, there is a huge variety of mixed oxygen ion and electron conductive perovskite compositions which have been published so far,[77] the most prominent example being lanthanum strontium cobalt ferrate or $La_{1-x}Sr_xCo_{1-y}Fe_yO_3$ (LSCF),[78] which is a chemically stable and already widely applied oxygen ion conductor, and the related $Ba_{1-x}Sr_xCo_{1-y}Fe_yO_3$ (BSCF). Compared to the proton conductive perovskites, both LSCF and BSCF show a very high electron conductivity, making them ideal materials for oxygen permeation membranes or electrodes in solid oxide fuel cells.[77,79] Grain boundaries within LSCF and BSCF are characterized by segregation of Sr and Ba, which are mobile within the crystal structure at common application temperatures, but also, depending on the exact composition, by segregation of Co cations.[80] However, there are no comprehensive AFM-based

measurements of the height and extent of the potential barrier in corresponding materials.

### 3.2 Doped ceria and yttria-stabilized zirconia

As doped ceria as well as YSZ show ionic conductivities combined with – in case of ceria – a considerable electronic conductivity depending on the dopant, they have already been object of intense investigations. Due to the fluorite structure of both materials, physical and electrochemical characteristics are isotropic within a crystal.

Previous studies confirmed that grain boundaries in acceptor doped ceria as well as YSZ[13,81–84] can be described as double-Schottky layer, with the grain boundary core being positively charged with respect to the grain interior. The positive charge of the grain boundary core is thought to be counterbalanced by a diffuse SCL of negative charge (electrons or small polarons), which extends into the bulk of the grain similar to the structure confirmed for proton conductive oxides.

For YSZ, the positive net charge of the grain boundary core was found to be mainly produced by segregation of immobile oxygen vacancies,[81] while for 10 cat% Gd-doped ceria an enrichment of $Gd^{3+}$ in the first cation layer and an enrichment of positively charged, immobile oxygen vacancies ($V_O^{\circ\circ}$) in the first anion layer of the grain surface was proposed based on simulations.[85] In the surrounding SCL, a decreased concentration of mobile $V_O^{\circ\circ}$ is found, while at the same time, the concentration of electrons is increased to compensate the positive net charge of the grain boundary core.[84,86] The simulations were confirmed by a variety of AFM-based experiments: direct measurements of the grain boundary potential barrier by KPFM have already successfully been achieved for Gd-doped ceria[87,88] confirming a potential barrier height in the area between 100–200 mV for 10 cat% acceptor doping, but strongly variable on a local scale depending on dopant concentration, inhomogeneities, crystal orientation *etc.* As can be seen from Fig. 3, the potential difference between grains and grain boundaries in 20 cat% Gd-doped ceria can still be perceived, but at a significantly reduced level. This is attributed to the phenomenon of reciprocal cancellation of effects at high dopant concentrations. In addition, combined polarization-KPFM measurements have been carried out on doped ceria and YSZ, which were used for the investigation of the surface exchange and local reduction–re-oxidation processes[89–91] as well as gathering information about the effect of grain boundaries by comparison of the polarization–relaxation characteristics of nanocrystalline and epitaxial ceria thin films.[92]

Doria *et al.*[93] compared the effects of polarization between nanocrystalline and epitaxial Sm-doped ceria thin films using

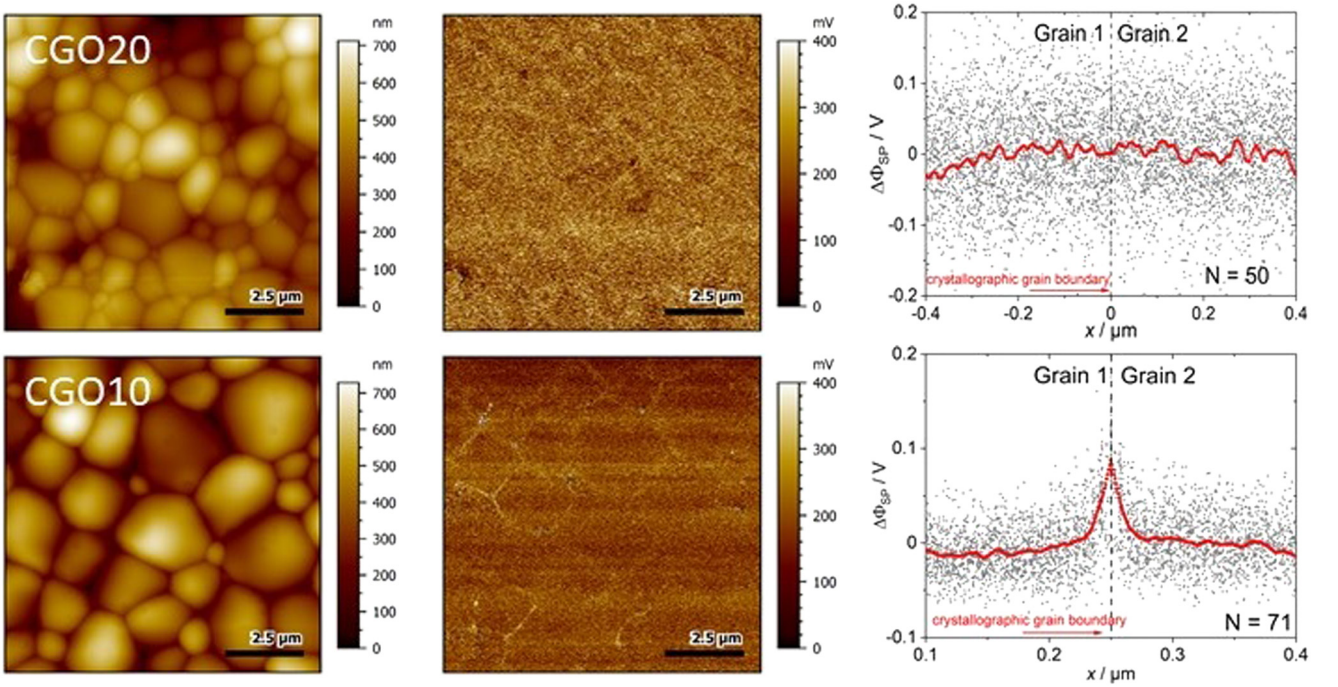


Fig. 3 Top left: Topography measurements of 20 cat% doped CGO (Sigma Aldrich, USA), top middle: corresponding surface potential measurement by KPFM, where grain boundaries can be observed as faint outline with higher potential, top right: average grain boundary potential for 50 grain boundaries, the grain boundary potential barrier is in the range of the noise. Bottom left: Topography measurements of 10 cat% doped CGO (Treibacher Industrie AG, Germany), bottom middle corresponding surface potential measurement by KPFM, where grain boundaries can be observed as clear outline with higher potential, bottom right: average grain boundary potential for 71 grain boundaries. The average grain boundary potential barrier height is about 100 mV. Both samples were measured as received using Pt-coated cantilevers (PPP-NCSTPt) with amplitude modulation mode in lab air.

ESM. By measuring the local vertical strain during application of short bias pulses and the subsequent mechanical relaxation of the samples, which relate directly to changes in the local defect concentration, they were able to show the existence of space-charge regions at Sm-doped ceria grain boundaries as well as at the sample surface with high resolution. The results were later backed up by measurements by Chen *et al.*, who used a similar measurement method at temperatures between 20–200 °C.[94]

### 3.3 ZnO – high electron conductivity paired with low proton conductivity

Pure ZnO is a cheap, non-toxic, transparent, n-type semiconductive material for multi-purpose application,[95,96] which also shows a slight proton conductivity. Historically, it has been commercially used as a pigment since the 19th century.[97] In electronics, ZnO ceramics and thin films are additionally widely used for photovoltaic and light emitting applications[98] and have also been proposed as material for other electronic components,[96,99] especially LEDs.[100,101] Apart from this, one of the most important applications of ZnO with additions of $Bi_2O_3$ and other oxides is as varistor material,[102] as it shows highly nonlinear I–V-properties, which are caused by double-Schottky barriers formed at the grain boundaries of the material.[103] Below a critical breakdown voltage, which is typically in the range of 3–4 V, charge transport across grain boundaries is almost purely capacitive and the boundary behaves like an insulator. Above the critical voltage, however, electron transport across the grain boundary becomes ohmic.

It is already known that negative charges represented by cation vacancies $V'_{Zn}$ and $V''_{Zn}$ segregate at the grain boundary, while a positively charged SCL surrounds the grain boundary, including mainly oxygen vacancies ($V_O^{\circ}$, $V_O^{\circ\circ}$) and zinc on interstitial lattice sites ($Zn_i^{\circ}$, $Zn_i^{\circ\circ}$), but also impurity donor cations at the place of Zn ($D_{Zn}^{\circ}$, *cf.* Fig. 4).[103,104] These cations can either be donor dopants or impurities like Bi or Sb, but

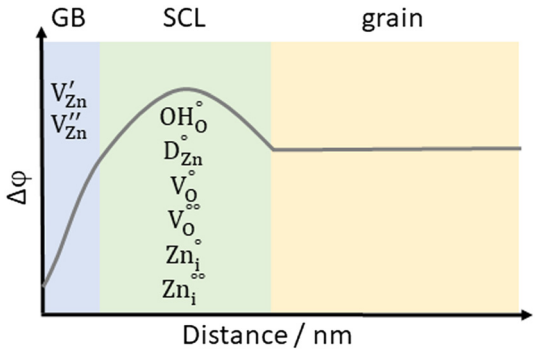


Fig. 4 Scheme of the local Volta potential distribution at the grain boundary of ZnO, showing a complex interplay of different types of charged defects which are mobile to different extents. At the grain boundary, negative defects are abundant, while in the adjacent positive depletion layer, an increased concentration of positive defects can be found.

it has been shown that protons or rather OH-groups at oxygen sites ($OH_O^{\circ}$) work as shallow donors in ZnO,[105–107] increasing the electronic conductivity.

AFM-based impedance spectroscopy methods have first been demonstrated using commercial ZnO varistor materials.[58,59] It was found that a parallel resistor–capacitor equivalent circuit associated with transport in the grain boundary in addition to the Schottky contact build by the metallic tip and surface, provides the best description of the impedance spectroscopy data, which was to be expected from macroscopic results.

It has been shown by KPFM measurements that the potential barrier height at the grain boundaries of ZnO is strongly depending on the synthesis process,[108] structure of the crystallites[109] and substrate in case of thin films.[110] For example Gonzalez-Julian *et al.*[108] reported that an increase of the total proton concentration in a sample by wetting during sample synthesis (in this case spark plasma sintering) leads to an increase of positive charge in the space-charge region and also to an increase of negative charge in the direct vicinity of the grain boundary. This resulted in an increased potential barrier at grain boundaries and increased electronic conductivity along the grain boundaries. The results were confirmed by macroscopic impedance spectroscopy measurements.

Further, de Lucas-Gil *et al.*[109] showed that by formation of star-shaped ZnO-particles consisting of stacked thin ZnO micro-platelets, the Schottky barrier character of the grain boundaries can be used to create negative charge accumulations by accumulating the band bending effect at the grain boundaries. The tips of the "stars" show an extremely high surface potential difference of up to 3.5 V between bulk and tips, which makes these particles suitable for antimicrobial applications. Similarly, Moreira *et al.*[110] were able to confirm using a combination of EFM, KPFM and CAFM band bending in the range of 50 meV at grain boundaries of ZnO thin films.

## 4 Lithium ion conductors

From the previous section, it can be concluded that consistent results for the analysis of charge transport and the potential barrier at grain boundaries can be achieved in both oxide-ion or proton conducting oxide electrolytes and mixed ionic/electronic conductive (MIEC) using conventional and AFM-based measurement techniques. The AFM-based measurement methods, which have so far been used more as niche applications, are therefore a valid instrument for carrying out detailed spatially resolved analyses at grain boundaries and should also be recognized as such by the community. In the following, we would like to show that this can also be utilized for lithium-ion conducting materials, which are much more in the scientific and industrial focus.

One of the key challenges for the design of efficient and long-living lithium batteries is to keep up a homogeneous Li-ion flow throughout several hundred charge and discharge

cycles and throughout the full reaction area to prevent inhomogeneous lithium deposition, which is frequently called Li metal dendrite formation, which is a severe problem for battery safety. One reason for inhomogeneities of the lithium ion distribution can be internal interfaces in the solid electrolyte or electrode materials,[111] for example grain boundaries and boundaries between different phases in composite materials. Investigation of local chemical, electrochemical and physical aspects can therefore help to improve the material design and battery safety.

Lithium ion conductors, similar to other ion conductors, can be divided in purely ion conductive (electrolyte) materials and MIEC materials, which are commonly used as active materials in lithium battery electrodes. Apart from this, the way of lithiation plays an important role: for layered materials like lithium cobalt oxide or NMC, $Li^+$ is intercalated and de-intercalated, while for the electrolyte lithium lanthanum titanate or high-voltage spinels like lithium manganese oxide, $Li^+$ can be inserted or de-inserted on lithium vacancies within the crystal structure (solid solution). In both cases, grain boundaries can either be disruptive or supportive for lithium transport.

For typical battery applications, however, active materials in particular are not installed as a block in the electrode but normally particles are mixed with carbon and a binder and this mix is applied to a current collector serving as substrate for the mix. For such applications, grain boundaries in the materials tend to play a subordinate role, but can nevertheless be of importance for instance in crack formation which is accompanied by capacity loss,[112,113] dendrite formation, or general ageing of the material. Still, the prevalent use of particles as well as the high moisture sensitivity of most battery materials are part of the reasons why there are even fewer studies dealing specifically with AFM-based measurements at grain boundaries for lithium-ion conductors than for the previously discussed oxidic materials.

### 4.1 Insertion materials

$Li_{3x}La_{0.67-x}TiO_3$ (LLTO) is an oxidic perovskite material that was first mentioned in the 1980s[114,115] and which exhibits very high lithium-ion conductivity.[116–121] The best conductivity with about 1 mS $cm^{-1}$ has been found for a composition of $Li_{0.3}La_{0.57}TiO_3$.[122] Therefore, the material has since been carefully investigated for applications in lithium ion batteries[122] but also for pH sensor application.[123–126] AFM measurements of LLTO samples were performed by Roffat *et al.*[127] to establish why LLTO shows either sensitivity or insensitivity to the pH of the environment depending on the sintering temperature. For all observed materials, the grain boundaries (which were not specifically addressed in this study) show a distinctly lower surface potential than the grain interior. Sasano *et al.* used AFM combined with atomic-resolution scanning transmission electron microscopy to study Li-ion conductivity at LLTO grain boundaries. The study found that certain grain boundaries reduce Li-ion conductivity due to positive charge formation and Li-ion depletion layers.[128,129]

The garnet-type material $Li_7La_3Zr_2O_{12}$ (LLZO) is another example for an oxide insertion-type electrolyte with high lithium-ion conductivity.[130,131] Lu *et al.* used LLZO as a model to show significant local inhomogeneity with a hundredfold decrease in dendrite triggering bias at grain boundaries compared to grain interiors using CAFM.[132] A small difference in the range of 25 mV can also be observed in KPFM measurements (*cf.* Fig. 5).

$ZnFe_2O_4$ is a material with spinel structure that has been discussed as a possible active material for the negative electrode in lithium-ion batteries as well as potential candidate for the positive electrode in zinc-ion batteries. Apart from this, it is in the focus of research due to its high photocatalytic activity and interesting magnetic properties. Recent measurements of the potential difference between grains and grain boundaries by KPFM show a similar difference as for LLZO.[133]

### 4.2 Layered intercalation materials

Lithium cobalt oxide ($Li_xCoO_2$) is a typical layered material, where $Li^+$ ions are intercalated or de-intercalated rather than solved in a solid solution. $Li_xCoO_2$ exhibits a strong correlation between its lithium content and the lattice parameters, making it an ideal material for ESM studies.[134] Balke *et al.*[48] showed that the $Li^+$ ion concentration within the material can be changed on a local scale by application of a constant voltage to the AFM tip. Using ESM to measure the local $Li^+$ ion transport, it was revealed that the $Li^+$ ion diffusivity is dependent on the crystallographic orientation of the respective grains. The orientation of the adjacent grains was found to influence the $Li^+$ ion transport behavior of the grain boundaries. The local conductance has therefore to be closely associated with localized $Li^+$ deficiency. Measurements by Zhu *et al.*[135] are in good accordance to these findings. They observed by means of CAFM that the grain boundaries in $Li_xCoO_2$ generally show an increased $Li^+$ ion diffusion due to a decreased potential barrier compared to the grains, which is beneficial for $Li^+$ ion transport. The experimental findings are also in accord to their first principle calculations. It was concluded that high-rate charge lithium ion batteries with a high capacity can be achieved by adapting $Li_xCoO_2$ nanostructured electrodes composed of grains with a large grain boundary to grain ratio.

Compared to $Li_xCoO_2$, $Li_aMn_xNi_yCo_zO_2$ (NMCxyz) shows a higher cost and performance effectiveness and can be tailored especially for high power or high energy applications. Yang *et al.* applied CAFM to measure the locally resolved conductivity of a $Li_{1.2}Co_{0.13}Ni_{0.13}Mn_{0.54}O_2$ thin films under different electric fields.[136] With increased applied voltage, the current flow at the grain boundaries increased significantly, while the current flow measured at the grain surfaces only increased moderately (*cf.* Fig. 6). Similar to $Li_xCoO_2$, the authors determined an increased $Li^+$ diffusion at

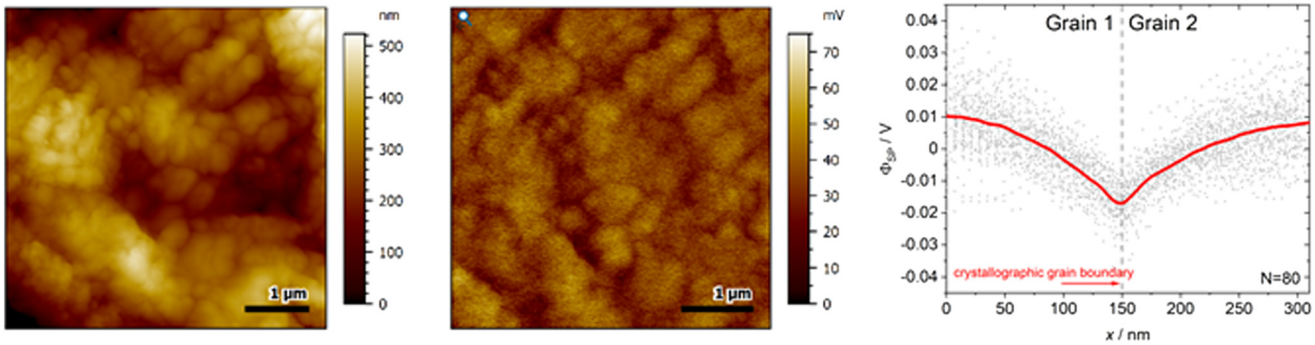


**Fig. 5** KPFM measurements on an untreated LLZO ceramic pellet. The sample was investigated using Pt-coated cantilevers (PPP-NCSTPt) with frequency modulation mode under glovebox atmosphere (Ar). Left: Topography measurements showing individual grains, middle: corresponding surface potential measurement where grain boundaries can be observed as faint outline with lower potential, right: average grain boundary potential for 80 grain boundaries. The average grain boundary potential difference is about 25 mV.

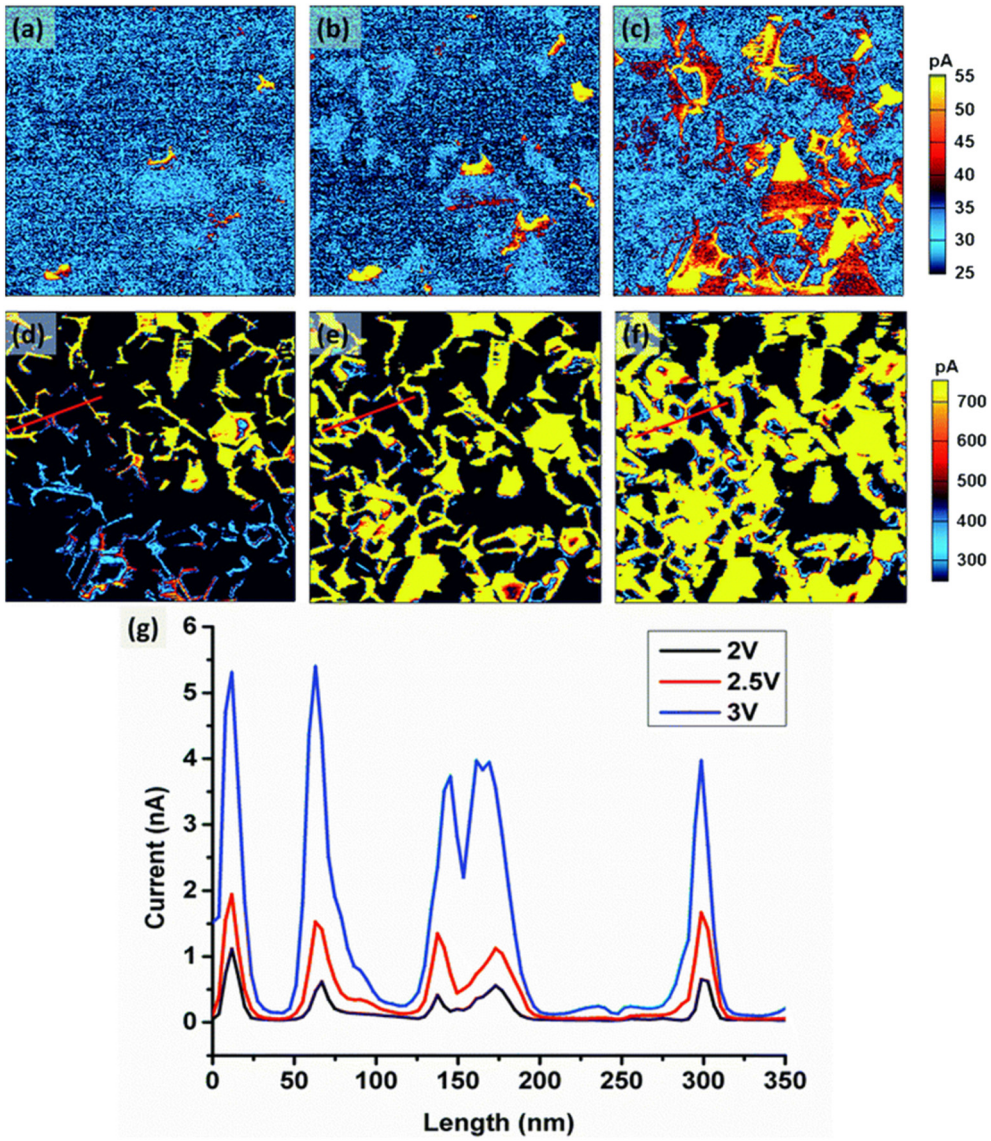


**Fig. 6** The changes of the current in $Li_{1.2}Co_{0.13}Ni_{0.13}Mn_{0.54}O_2$ cathode thin film under various electrical fields over the scanning area of 1.5 × 1.5 $\mu m^2$. (a) to (f) are the current images scanned with the bias of 0.5 V, 1 V, 1.5 V, 2 V, 2.5 V and 3 V, respectively; and (g) is the current profile along the lines in the images (d) to (f), respectively. Image and caption taken from ref. 136 (Creative Commons license CC BY 3.0).

grain boundaries for this NMC composition, which is associated with a lower diffusion energy barrier for $Li^+$ ions compared to the bulk of the grain.

In summary there have been first promising studies on the use of AFM-based measurement methods for the analysis of grain boundaries are also available in the field of lithium ion conductors. Particularly for issues in all-solid-state batteries, corresponding measurement techniques can provide interesting and further impulses for research.

## 5 Conclusions and future perspectives

AFM-based electrochemical measurement methods are well-suited to give detailed information about the charge carrier transport characteristics at grain boundaries with very high local resolution. By complementing other imaging methods like electron microscopy methods, various vibrational spectroscopy methods or cathodoluminescence as well as a broad range of macroscopic electrochemical experiments, AFM-based methods have become more common in electrochemical analysis but however, are still rarely used.

A major disadvantage of AFM measurements is that they usually only provide information about the top few nm of the surface. Some deviation from the behavior of the bulk material is to be expected, especially when additional preparation techniques such as polishing *etc.* are used, which may introduce additional (immobile) defects or contamination. Therefore, complementary measurements using bulk techniques such as impedance spectroscopy are still essential for a complete description of the grain boundaries in a sample. In addition, it must always be considered that AFM measurements take place at a boundary to the gas phase or vacuum and therefore a different defect distribution and activity is to be expected than in the bulk. Conversely, this represents a key advantage of AFM-based measurement techniques, especially for oxide-ion and proton-conducting materials, as it is possible to study the surface exchange in different gas environments in more detail. The same holds true for lithium-ion conducting materials, as they can be studied in direct contact to liquid electrolytes which mainly is not possible with other high-resolution imaging methods.

Similar to grain boundaries, other interfaces in a given material can of course be investigated by AFM – as is already done in photovoltaics. Regions of interest for AFM-based electrochemical characterizations for example in battery research could be interphases, *i.e.* the solid electrolyte interphase (SEI) at the anode side or cathode electrolyte interphase (CEI) as well as interfaces in hybrid electrolyte materials[137] or electrode composites. Published measurements include several *in situ* and *operando* measurement setups and already yield valuable results. Other areas of interest are of course fuel cell materials and especially catalytic reactions at MIEC surfaces, for example for membrane reactor applications, as well as oxygen or proton permeation membranes ($O_2$ and $H_2$ splitting and incorporation, methanation of $CO_2$ syngas formation, *etc.*).

Generally speaking, it can be said that although AFM-based measurement techniques enable a wide range of possible measured variables, these possibilities are still far from being widely applied in "classical" defect chemical and electrochemical research.

## Data availability

No primary research results, software or code have been included and no new data were generated or analysed as part of this review.

## Conflicts of interest

There are no conflicts to declare.

## Acknowledgements

The authors acknowledge funding by the German Research Foundation (DFG) – project #387282673.

## References

1 G. Binnig, C. F. Quate and C. Gerber, *Phys. Rev. Lett.*, 1986, **56**, 930.
2 F. J. Giessibl, *Rev. Mod. Phys.*, 2003, **75**, 949.
3 M. Setvín, M. Wagner, M. Schmid, G. S. Parkinson and U. Diebold, *Chem. Soc. Rev.*, 2017, **46**, 1772–1784.
4 P. Bampoulis, R. van Bremen, Q. Yao, B. Poelsema, H. J. Zandvliet and K. Sotthewes, *ACS Appl. Mater. Interfaces*, 2017, **9**, 19278–19286.
5 C. Maragliano, S. Lilliu, M. Dahlem, M. Chiesa, T. Souier and M. Stefancich, *Sci. Rep.*, 2014, **4**, 4203.
6 L. Yang, Y. Wang, X. Wang, S. Shafique, F. Zheng, L. Huang, X. Liu, J. Zhang, Y. Zhu and C. Xiao, *Small*, 2024, **20**, 2304362.
7 C. C. Ahia and E. L. Meyer, *Phys. Status Solidi A*, 2024, **221**, 2300293.
8 J. Frenkel, *Kinetic Theory Of Liquids*, Clarendon Press, Oxford, 1946.
9 C. Wagner, *J. Phys. Chem. Solids*, 1972, **33**, 1051–1059.
10 J. B. Wagner and T. Jow, *J. Electrochem. Soc.*, 1979, **126**, 163.
11 S. Kim and J. Maier, *J. Eur. Ceram. Soc.*, 2004, **24**, 1919–1923.
12 J. Maier, *Prog. Solid State Chem.*, 1995, **23**, 171–263.
13 X. Guo, W. Sigle, J. Fleig and J. Maier, *Solid State Ionics*, 2002, **154–155**, 555–561.
14 S. Kim, J. Fleig and J. Maier, *Phys. Chem. Chem. Phys.*, 2003, **5**, 2268–2273.
15 J. Maier, *Ber. Bunsenges. Phys. Chem.*, 1989, **93**, 1468–1473.
16 J. Maier, *Ber. Bunsenges. Phys. Chem.*, 1985, **89**, 355–362.
17 J. Maier, *J. Phys. Chem. Solids*, 1985, **46**, 309–320.
18 J. Maier, S. Prill and B. Reichert, *Solid State Ionics*, 1988, **28–30**, 1465–1469.
19 S. Kim, *Phys. Chem. Chem. Phys.*, 2016, **18**, 19787–19791.

20 D. R. Diercks, J. Tong, H. Zhu, R. Kee, G. Baure, J. C. Nino, R. O'Hayre and B. P. Gorman, *J. Mater. Chem. A*, 2016, **4**, 5167–5175.
21 K. Sato, *J. Phys. Chem. C*, 2015, **119**, 5734–5738.
22 H. B. Lee, F. B. Prinz and W. Cai, *Acta Mater.*, 2013, **61**, 3872–3887.
23 A. Tschöpe, S. Kilassonia and R. Birringer, *Solid State Ionics*, 2004, **173**, 57–61.
24 S. K. Kim, S. Khodorov, I. Lubomirsky and S. Kim, *Phys. Chem. Chem. Phys.*, 2014, **16**, 14961–14968.
25 D. S. Mebane and R. A. De Souza, *Energy Environ. Sci.*, 2015, **8**, 2935–2940.
26 N. Shibata, Y. Ikuhara, F. Oba, T. Yamamoto and T. Sakuma, *Philos. Mag. Lett.*, 2002, **82**, 393–400.
27 X. Xu, Y. Liu, J. Wang, D. Isheim, V. P. Dravid, C. Phatak and S. M. Haile, *Nat. Mater.*, 2020, 1–7.
28 S.-Y. Park, P.-S. Cho, S. B. Lee, H.-M. Park and J.-H. Lee, *J. Electrochem. Soc.*, 2009, **156**, B891.
29 G. Lewis, A. Atkinson, B. Steele and J. Drennan, *Solid State Ionics*, 2002, **152**, 567–573.
30 H. J. Avila-Paredes and S. Kim, *Solid State Ionics*, 2006, **177**, 3075–3080.
31 S. Kim, S. Khodorov, L. Chernyak, T. Defferriere, H. Tuller and I. Lubomirsky, *Solid State Ionics*, 2024, **417**, 116706.
32 L. Katzenmeier, L. Carstensen and A. S. Bandarenka, *ACS Appl. Mater. Interfaces*, 2022, **14**, 15811–15817.
33 K. V. Hansen, C. Sander, S. Koch and M. Mogensen, *J. Phys.: Conf. Ser.*, 2007, **61**, 389.
34 K. V. Hansen, Y. Wu, T. Jacobsen, M. B. Mogensen and L. T. Kuhn, *Rev. Sci. Instrum.*, 2013, **84**(7), 073701.
35 Z. Zhang, S. Said, K. Smith, R. Jervis, C. A. Howard, P. R. Shearing, D. J. Brett and T. S. Miller, *Adv. Energy Mater.*, 2021, **11**, 2101518.
36 S. V. Kalinin and N. Balke, *Adv. Mater.*, 2010, **22**, E193–E209.
37 A. N. Morozovska, E. A. Eliseev, N. Balke and S. V. Kalinin, *J. Appl. Phys.*, 2010, **108**, 053712.
38 S. V. Kalinin, N. Balke, S. Jesse, A. Tselev, A. Kumar, T. M. Arruda, S. Guo and R. Proksch, *Mater. Today*, 2011, **14**, 548–558.
39 S. Kim, K. No and S. Hong, *Chem. Commun.*, 2016, **52**, 831–834.
40 D. O. Alikin, A. V. Ievlev, S. Y. Luchkin, A. P. Turygin, V. Y. Shur, S. V. Kalinin and A. L. Kholkin, *Appl. Phys. Lett.*, 2016, **108**, 113106.
41 D.-W. Chung, N. Balke, S. V. Kalinin and R. E. Garcia, *J. Electrochem. Soc.*, 2011, **158**, A1083.
42 S. Yang, B. Yan, J. Wu, L. Lu and K. Zeng, *ACS Appl. Mater. Interfaces*, 2017, **9**, 13999–14005.
43 Q. N. Chen, Y. Liu, Y. Liu, S. Xie, G. Cao and J. Li, *Appl. Phys. Lett.*, 2012, **101**, 063901.
44 A. Kumar, S. Jesse, A. N. Morozovska, E. Eliseev, A. Tebano, N. Yang and S. V. Kalinin, *Nanotechnology*, 2013, **24**, 145401.
45 A. Kumar, F. Ciucci, A. N. Morozovska, S. V. Kalinin and S. Jesse, *Nat. Chem.*, 2011, **3**, 707–713.
46 F. Hausen and N. Balke, *Curr. Opin. Electrochem.*, 2024, 101562.
47 S. Jesse, A. Kumar, T. M. Arruda, Y. Kim, S. V. Kalinin and F. Ciucci, *MRS Bull.*, 2012, **37**, 651–658.
48 N. Balke, S. Jesse, A. N. Morozovska, E. Eliseev, D. W. Chung, Y. Kim, L. Adamczyk, R. E. Garcia, N. Dudney and S. V. Kalinin, *Nat. Nanotechnol.*, 2010, **5**, 749–754.
49 M. Nonnenmacher, M. P. O'Boyle and H. K. Wickramasinghe, *Appl. Phys. Lett.*, 1991, **58**, 2921–2923.
50 M. Nonnenmacher, M. O'Boyle and H. K. Wickramasinghe, *Ultramicroscopy*, 1992, **42–44**, 268–273.
51 W. Melitz, J. Shen, A. C. Kummel and S. Lee, *Surf. Sci. Rep.*, 2011, **66**, 1–27.
52 T. Mélin, M. Zdrojek and D. Brunel, in *Scanning Probe Microscopy in Nanoscience and Nanotechnology*, ed. B. Bhushan, Springer, Berlin, 1st edn, 2010, pp. 89–128.
53 U. Zerweck, C. Loppacher, T. Otto, S. Grafström and L. M. Eng, *Phys. Rev. B: Condens. Matter Mater. Phys.*, 2005, **71**, 125424.
54 H. O. Jacobs, P. Leuchtmann, O. J. Homan and A. Stemmer, *J. Appl. Phys.*, 1998, **84**, 1168–1173.
55 K. Schmale, J. Barthel, M. Bernemann, M. Grünebaum, S. Koops, M. Schmidt, J. Mayer and H. D. Wiemhöfer, *J. Solid State Electrochem.*, 2013, **17**, 2897–2907.
56 C. Örnek, C. Leygraf and J. Pan, *Corros. Eng., Sci. Technol.*, 2019, **54**, 185–198.
57 S. V. Kalinin and D. A. Bonnell, *Appl. Phys. Lett.*, 2001, **78**, 1306–1308.
58 R. Shao, S. V. Kalinin and D. A. Bonnell, *Appl. Phys. Lett.*, 2003, **82**, 1869–1871.
59 R. O'Hayre, M. Lee and F. B. Prinz, *J. Appl. Phys.*, 2004, **95**, 8382–8392.
60 L. Lei, R. Xu, S. Ye, X. Wang, K. Xu, S. Hussain, Y. J. Li, Y. Sugawara, L. Xie and W. Ji, *J. Phys. Commun.*, 2018, **2**, 025013.
61 O. Amster, Y. Yang, B. Drevniok, S. Friedman, F. Stanke and S. J. Dixon-Warren, Practical quantitative scanning microwave impedance microscopy of semiconductor devices, *2017 IEEE 24th International Symposium on the Physical and Failure Analysis of Integrated Circuits (IPFA)*, 2017, pp. 1–4.
62 M. Tuteja, P. Koirala, V. Palekis, S. MacLaren, C. S. Ferekides, R. W. Collins and A. A. Rockett, *J. Phys. Chem. C*, 2016, **120**, 7020–7024.
63 J. Myers, T. Nicodemus, Y. Zhuang, T. Watanabe, N. Matsushita and M. Yamaguchi, *J. Appl. Phys.*, 2014, **115**, 17A506.
64 J. Zhu, C. R. Pérez, T.-S. Oh, R. Küngas, J. M. Vohs, D. A. Bonnell and S. S. Nonnenmann, *J. Mater. Res.*, 2015, **30**, 357–363.
65 K. Sasaki and J. Maier, *J. Appl. Phys.*, 1999, **86**, 5422–5433.
66 K. Sasaki and J. Maier, *J. Appl. Phys.*, 1999, **86**, 5434–5443.
67 H. J. Avila-Paredes, C.-T. Chen, S. Wang, R. A. De Souza, M. Martin, Z. Munira and S. Kim, *J. Mater. Chem.*, 2010, **20**, 10110–10112.
68 G. Gregori, M. Shirpour and J. Maier, *Adv. Funct. Mater.*, 2013, **23**, 5861–5867.
69 C. Tandé, D. Pérez-Coll and G. C. Mather, *J. Mater. Chem.*, 2012, **22**, 11208–11213.

70 J. S. Park, Y. B. Kim, J. H. Shim, S. Kang, T. M. Gür and F. B. Prinz, *Chem. Mater.*, 2010, **22**, 5366–5370.
71 C. Kjølseth, H. Fjeld, Ø. Prytz, P. I. Dahl, C. Estournès, R. Haugsrud and T. Norby, *Solid State Ionics*, 2010, **181**, 268–275.
72 S. Duval, P. Holtappels, U. Vogt, E. Pomjakushina, K. Conder, U. Stimming and T. Graule, *Solid State Ionics*, 2007, **178**, 1437–1441.
73 M. Shirpour, B. Rahmati, W. Sigle, P. A. van Aken, R. Merkle and J. Maier, *J. Phys. Chem. C*, 2012, **116**, 2453–2461.
74 P. Babilo, T. Uda and S. M. Haile, *J. Mater. Res.*, 2007, **22**, 1322–1330.
75 N. Yang, C. Cantoni, V. Foglietti, A. Tebano, A. Belianinov, E. Strelcov, S. Jesse, D. Di Castro, E. Di Bartolomeo, S. Licoccia, S. V. Kalinin, G. Balestrino and C. Aruta, *Nano Lett.*, 2015, **15**, 2343–2349.
76 J. Ding, J. Balachandran, X. Sang, W. Guo, G. M. Veith, C. A. Bridges, C. M. Rouleau, J. D. Poplawsky, N. Bassiri-Gharb, P. Ganesh and R. R. Unocic, *ACS Appl. Mater. Interfaces*, 2018, **10**, 4816–4823.
77 J. Sunarso, S. Baumann, J. M. Serra, W. A. Meulenberg, S. Liu, Y. S. Lin and J. C. Diniz Da Costa, *J. Membr. Sci.*, 2008, **320**, 13–41.
78 Y. Teraoka, H. M. Zhang, K. Okamoto and N. Yamazoe, *Mater. Res. Bull.*, 1988, **23**, 51–58.
79 S. Baumann, J. M. Serra, M. P. Lobera, S. Escolástico, F. Schulze-Küppers and W. A. Meulenberg, *J. Membr. Sci.*, 2011, **377**, 198–205.
80 X. Wang, T. Miyazaki, K. Yashiro, S. Hashimoto and T. Kawada, *ECS Trans.*, 2017, **75**, 1–9.
81 J. An, J. S. Park, A. L. Koh, H. B. Lee, H. J. Jung, J. Schoonman, R. Sinclair, T. M. Gür and F. B. Prinz, *Sci. Rep.*, 2013, **3**, 2680.
82 X. Guo, W. Sigle and J. Maier, *J. Am. Ceram. Soc.*, 2003, **86**, 77–87.
83 X. Guo and R. Waser, *Solid State Ionics*, 2004, **173**, 63–67.
84 X. Guo and R. Waser, *Prog. Mater. Sci.*, 2006, **51**, 151–210.
85 H. B. Lee, F. B. Prinz and W. Cai, *Acta Mater.*, 2010, **58**, 2197–2206.
86 R. Waser and R. Hagenbeck, *Acta Mater.*, 2000, **48**, 797–825.
87 K. Neuhaus and H.-D. Wiemhöfer, *Solid State Ionics*, 2021, **371**, 115771.
88 W. Lee, H. J. Jung, M. H. Lee, Y. B. Kim, J. S. Park, R. Sinclair and F. B. Prinz, *Adv. Funct. Mater.*, 2012, **22**, 965–971.
89 W. Lee, M. Lee, Y.-B. Kim and F. B. Prinz, *Nanotechnology*, 2009, **20**, 445706.
90 K. Neuhaus, M. Bernemann, K. V. Hansen, T. Jacobsen, G. Ulbrich, E. Heppke, M. Paun, M. Lerch and H.-D. Wiemhöfer, *J. Electrochem. Soc.*, 2016, **163**, H1179–H1185.
91 K. Neuhaus, F. Schulze-Küppers, S. Baumann, G. Ulbrich, M. Lerch and H.-D. Wiemhöfer, *Solid State Ionics*, 2016, **288**, 325–330.
92 K. Neuhaus, G. Gregori and J. Maier, *ECS J. Solid State Sci. Technol.*, 2018, **7**, P362.
93 S. Doria, N. Yang, A. Kumar, S. Jesse, A. Tebano, C. Aruta, E. Di Bartolomeo, T. M. Arruda, S. V. Kalinin and S. Licoccia, *Appl. Phys. Lett.*, 2013, **103**, 171605.
94 Q. N. Chen, S. B. Adler and J. Li, *Appl. Phys. Lett.*, 2014, **105**, 201602.
95 C. G. Van de Walle, *Phys. Rev. Lett.*, 2000, **85**, 1012.
96 B. Barros, R. Barbosa, N. dos Santos, T. Barros and M. Souza, *Inorg. Mater.*, 2006, **42**, 1348–1351.
97 L. Burgio, R. J. H. Clark and P. J. Gibbs, *J. Raman Spectrosc.*, 1999, **30**, 181–184.
98 J. E. Nause, *ZnO broadens the spectrum, III-Vs Review*, 1999, vol. 12(4), pp. 28–31.
99 T. K. Gupta, *J. Am. Ceram. Soc.*, 1990, **73**, 1817–1840.
100 X. Jiang, F. L. Wong, M. K. Fung and S. T. Lee, *Appl. Phys. Lett.*, 2003, **83**, 1875–1877.
101 Y. I. Alivov, E. V. Kalinina, A. E. Cherenkov, D. C. Look, B. M. Ataev, A. K. Omaev, M. V. Chukichev and D. M. Bagnall, *Appl. Phys. Lett.*, 2003, **83**, 4719–4721.
102 G. D. Mahan, *J. Appl. Phys.*, 1983, **54**, 3825–3832.
103 T. K. Gupta and W. G. Carlson, *J. Mater. Sci.*, 1985, **20**, 3487–3500.
104 A. F. Kohan, G. Ceder, D. Morgan and C. G. Van de Walle, *Phys. Rev. B: Condens. Matter Mater. Phys.*, 2000, **61**, 15019–15027.
105 C. G. Van de Walle, *Phys. Rev. Lett.*, 2000, **85**, 1012.
106 D. M. Hofmann, A. Hofstaetter, F. Leiter, H. Zhou, F. Henecker, B. K. Meyer, S. B. Orlinskii, J. Schmidt and P. G. Baranov, *Phys. Rev. Lett.*, 2002, **88**, 045504.
107 A. Janotti and C. G. Van de Walle, *Rep. Prog. Phys.*, 2009, **72**, 126501.
108 J. Gonzalez-Julian, K. Neuhaus, M. Bernemann, J. Pereira da Silva, A. Laptev, M. Bram and O. Guillon, *Acta Mater.*, 2018, **144**, 116–128.
109 E. de Lucas-Gil, J. J. Reinosa, K. Neuhaus, L. Vera-Londono, M. Martín-González, J. F. Fernández and F. Rubio-Marcos, *ACS Appl. Mater. Interfaces*, 2017, **9**, 26219–26225.
110 R. Moreira, L. P. dos Santos, C. Salomão, E. B. Barros and I. F. Vasconcelos, *ACS Appl. Electron. Mater.*, 2023, **6**, 415–425.
111 J. Kuriplach, A. Pulkkinen and B. Barbiellini, *Condens. Matter*, 2019, **4**, 80.
112 S. Lee, L. Su, A. Mesnier, Z. Cui and A. Manthiram, *Joule*, 2023, **7**, 2430–2444.
113 E. Trevisanello, R. Ruess, G. Conforto, F. H. Richter and J. Janek, *Adv. Energy Mater.*, 2021, **11**, 2003400.
114 A. G. Belous, G. N. Novitskaya, S. V. Polyanetskaya and Y. I. Gornikov, *Neorg. Mater.*, 1987, **23**, 470–547.
115 L. Latie, G. Villeneuve, D. Conte and G. Le Flem, *J. Solid State Chem.*, 1984, **51**, 293–299.
116 J.-G. Kim, H.-G. Kim and H.-T. Chung, *J. Mater. Sci. Lett.*, 1999, **18**, 493–496.
117 H. Kawai and J. Kuwano, *J. Electrochem. Soc.*, 1994, **141**, L78–L79.
118 E. E. Jay, M. J. D. Rushton, A. Chroneos, R. W. Grimes and J. A. Kilner, *Phys. Chem. Chem. Phys.*, 2015, **17**, 178–183.
119 J. Ibarra, A. Várez, C. León, J. Santamaría, L. M. Torres-Martínez and J. Sanz, *Solid State Ionics*, 2000, **134**, 219–228.

120 C. H. Chen and K. Amine, *Solid State Ionics*, 2001, **144**, 51–57.
121 O. Bohnke, C. Bohnke and J. L. Fourquet, *Solid State Ionics*, 1996, **91**, 21–31.
122 S. Stramare, V. Thangadurai and W. Weppner, *Chem. Mater.*, 2003, **15**, 3974–3990.
123 M. Vijayakumar, Q. N. Pham and C. Bohnke, *J. Eur. Ceram. Soc.*, 2005, **25**, 2973–2976.
124 C. Bohnke, B. Regrag, F. Le Berre, J. L. Fourquet and N. Randrianantoandro, *Solid State Ionics*, 2005, **176**, 73–80.
125 C. Bohnke and J.-L. Fourquet, *Electrochim. Acta*, 2003, **48**, 1869–1878.
126 C. Bohnke, H. Duroy and J. L. Fourquet, *Sens. Actuators, B*, 2003, **89**, 240–247.
127 M. Roffat, O. Noël, O. Soppera and O. Bohnke, *Sens. Actuators, B*, 2009, **138**, 193–200.
128 S. Sasano, R. Ishikawa, G. Sánchez-Santolino, H. Ohta, N. Shibata and Y. Ikuhara, *Nano Lett.*, 2021, **21**, 6282–6288.
129 S. Sasano, R. Ishikawa, K. Kawahara, T. Kimura, Y. H. Ikuhara, N. Shibata and Y. Ikuhara, *Appl. Phys. Lett.*, 2020, **116**, 043901.
130 M. M. Raju, F. Altayran, M. Johnson, D. Wang and Q. Zhang, *Electrochemistry*, 2021, **2**, 390–414.
131 L. Zhang, Q. Zhuang, R. Zheng, Z. Wang, H. Sun, H. Arandiyan, Y. Wang, Y. Liu and Z. Shao, *Energy Storage Mater.*, 2022, **49**, 299–338.
132 Z. Lu, Z. Yang, C. Li, K. Wang, J. Han, P. Tong, G. Li, B. S. Vishnugopi, P. P. Mukherjee and C. Yang, *Adv. Energy Mater.*, 2021, **11**, 2003811.
133 S. Krämer, J. Hopster, A. Windmüller, R.-A. Eichel, M. Grünebaum, T. Jüstel, M. Winter and K. Neuhaus, *Energy Adv.*, 2024, **3**, 2175.
134 G. Amatucci, J. Tarascon and L. Klein, *J. Electrochem. Soc.*, 1996, **143**, 1114.
135 X. Zhu, C. S. Ong, X. Xu, B. Hu, J. Shang, H. Yang, S. Katlakunta, Y. Liu, X. Chen and L. Pan, *Sci. Rep.*, 2013, **3**, 1–8.
136 S. Yang, B. Yan, L. Lu and K. Zeng, *RSC Adv.*, 2016, **6**, 94000–94009.
137 B. Wang, M. S. R. Limon, Y. Zhou, K. Cho, Z. Ahmad and L. Su, *ACS Energy Lett.*, 2025, **10**, 1255–1257.